ADVANCED FUNCTIONAL MATERIALS
www.afm-journal.de

Accelerating Materials Discovery by High-Throughput GIWAXS Characterization of Quasi-2D Formamidinium Metal Halide Perovskites

*Jonghee Yang, Juanita Hidalgo, Donghoon Song, Sergei V. Kalinin, Juan-Pablo Correa-Baena, and Mahshid Ahmadi**

The intriguing functionalities of emerging quasi-2D metal halide perovskites (MHPs) have led to further exploration of this material class for sustainable and scalable optoelectronic applications. However, the chemical complexities in precursors—primarily determined by the 2D:3D compositional ratio—result in uncontrolled phase heterogeneities in these materials, which compromises the optoelectronic performances. Yet, this phenomenon remains poorly understood due to the massive quasi-2D compositional space. To systematically explore the fundamental principles, herein, a high-throughput automated synthesis-characterization workflow is designed and implemented to formamidinium (FA)-based quasi-2D MHP system. It is revealed that the stable 3D-like phases, where the α-$FAPbI_3$ surface is passivated by 2D spacers, exclusively emerge at the compositional range (35–55% of $FAPbI_3$), deviating from the stoichiometric considerations. A quantitative crystallographic study via high-throughput grazing-incidence wide-angle X-ray scattering (GIWAXS) experiments integrated with automated peak analysis function quickly reveals that the 3D-like phases are vertically aligned, facilitating vertical charge conduction that can be beneficial for optoelectronic applications. Together, this study uncovers the optimal 2D:3D compositional range for complex quasi-2D MHP systems, realizing promising optoelectronic functionalities. The automated experimental workflow significantly accelerates materials discoveries and processing optimizations that are transferrable to other deposition methods, while providing fundamental insights into complex materials systems.

1. Introduction

Metal halide perovskites (MHPs) have gained extensive attention as materials platforms for next-generation optoelectronic applications including photovoltaics (PVs), light-emitting devices (LEDs), and neuromorphic electronics.[1–5] This is attributed to their excellent materials properties realizing high optoelectronic performances and facile solution processibility suited to scalable productions.[6] Nevertheless, one of the crucial bottlenecks retarding the ubiquitous applications of the MHPs in the real world is poor stability. The lability of the materials readily causes significant losses of the outstanding functionalities, which in turn become no longer suited to long-term sustainable applications.[7–9]

Quasi-2D MHPs have recently emerged as a promising materials class that shows significantly enhanced stability than 3D analogs.[10] Quasi-2D MHPs exhibit unique crystallographic structures that differentiate them from their 3D counterparts, where the large-sized organic cations, called spacers, confine the MHP crystal structure at the surface to be grown along 2D space.[11,12] This enables tuning of optoelectronic characteristics by thickness control of the confined structure—quantified by the number of the MHP monolayer (n) in the confined structure; it can be described as a chemical formula of $L_2A_{n-1}B_nX_{3n+1}$ (L, A, B and X are monovalent spacer cations, monovalent organic/inorganic cations, divalent metal cations and halides, respectively).[11,12] Additionally, the spacer cation can protect the functional phase structure against deformation via external stresses, thereby enhancing the phase stability compared to the 3D MHP counterparts—particularly, $FAPbI_3$-based systems.[10,13]

While the phase stability problem is significantly mitigated, still the optoelectronic performances of the quasi-2D MHP systems, particularly in PV applications, are lagging behind that of 3D.[14,15] This is attributed to the uncontrolled emergence of multiple quasi-2D phases in the films,[16] where such phase heterogeneity significantly compromises the carrier conduction properties.[17,18] In some specific cases, the phase heterogeneity

J. Yang, S. V. Kalinin, M. Ahmadi
Institute for Advanced Materials and Manufacturing
Department of Materials Science and Engineering
University of Tennessee
Knoxville, TN 37996, USA
E-mail: mahmadi3@utk.edu
J. Yang
Department of Chemistry
Yonsei University
Seoul 03722, Republic of Korea
J. Hidalgo, D. Song, J.-P. Correa-Baena
School of Materials Science and Engineering
Georgia Institute of Technology
Atlanta, GA 30332, USA

The ORCID identification number(s) for the author(s) of this article can be found under https://doi.org/10.1002/adfm.202409293

DOI: 10.1002/adfm.202409293

in quasi-2D MHPs can be evolved along the vertical direction of the films—3D-rich at the top, 2D-rich at the bottom of the MHP,[19,20] attributed to the imbalanced crystallization kinetics of 3D and 2D MHP components.[21]

In fact, the crystallization of quasi-2D MHPs—a chemically complex materials system—is largely dependent on multiple physio-chemical factors.[20,22–27] Particularly, the ratio of 2D:3D compositions in the MHP precursors primarily influences the final phase constitution of the quasi-2D MHP films.[21] Notwithstanding, so far, there is no consensus or fundamental guidelines for designing an optimal 2D:3D composition ratio within a wide range of MHP compositional spaces exhibiting promising optoelectronic functionalities. In fact, most publications demonstrating high-performance quasi-2D MHP optoelectronics have utilized various 2D:3D composition ratios, each of which strongly stems from the preliminary optimization process of each research group, but with a handful of basis sets.[16,28–30] Such inconsistency is now crucially decelerating the lab-to-fab transformation and realization of scalable manufacturing quasi-2D MHP optoelectronics in the real world.

Herein, we implement a high-throughput automated experimental workflow to systematically explore the phase heterogeneity of quasi-2D MHPs as a function of 2D:3D compositional ratios.[21,31] By using a robotic pipetting platform, an array of 96 quasi-2D MHP films are quickly synthesized, and the phase distributions and their time-evolution in each film—along the vertical directions and compositional changes—are autonomously characterized via photoluminescence (PL) spectroscopy. A machine learning (ML)-based analysis effectively reveals the compositional and geometric constitutions of the associated phases in the system from the massive PL dataset, the amount of which is impossible for individuals to manually analyze.

In this study, we specifically selected the phenethylammonium (PEA) and formamidinium (FA)-based quasi-2D MHP system, which shows promising functionalities although suffering from thermodynamic instability of functional α-$FAPbI_3$ phase that causes phase heterogeneities.[1,13,23,26,32,33] We observe that 3D-like phases, α-$FAPbI_3$ MHPs where the phase stability is enhanced by surface passivation of PEA cations,[10] exclusively emerge in the 2D:3D compositional space of 35–55% of $FAPbI_3$ ratio. Note that this compositional range far deviates from the stoichiometric considerations, which is difficult to manually predict by chemical intuitions based on the handful of experiments.[13,24]

We further explore the evolution of crystallographic structures and orientations of the MHP phases in the quasi-2D compositional space via high-throughput grazing-incidence wide-angle X-ray scattering (GIWAXS) experiments, allowing the comprehensive structural understanding of the functional materials system. Here, an automated peak analysis function is implemented for analyzing 285 individual GIWAXS patterns,[21] not only accelerating the overall materials discovery sequence but also uncovering the global trends of phase constitutions, vertical distributions, and, orientations in the complex system. Our analysis revealed that vertically aligned α-$FAPbI_3$ MHPs emerge at the compositional range exactly where the PL of the stable 3D-like phases is observed; this is also corroborated by PV performance assessment where the MHP film with 60% 3D reproducibly produces the highest photocurrent indeed. The joint high-throughput explorations of quasi-2D MHPs clearly uncover the optimal 2D:3D ratios for desired functionalities with structural insights, thereby providing a guideline required for the design of functional systems.

Our study exemplifies how a high-throughput synthesis-characterization workflow can effectively accelerate the discoveries of complex material systems exhibiting multiple functionalities and the sequence of processing optimizations, which can also be universally compatible with other deposition techniques. Moreover, these findings provide comprehensive insights into the fundamental principles controlling the phase constitutions in the quasi-2D MHPs, which is vital for designing functional systems that can be directly implemented in scalable manufacturing processes.

2. Results and Discussion

Various studies have explored the crystallization behavior and the resulting phase distributions in quasi-2D MHP systems, revealing that multiple parameters and factors, including solvent-solute interactions, crystallization rates, ion diffusion behaviors, and temperatures, can sensitively affect the resulting system.[20,22–27] Among them, the most intuitive determinant controlling the final phase distributions of quasi-2D MHPs is the ratio of 2D:3D compositions.[21] Nevertheless, there is no generalized principle on how to design the quasi-2D MHP system with an optimal 2D:3D ratio for high-performance MHP optoelectronics, even though many publications have already demonstrated excellent device performances. In fact, the exploration of the optimal 2D:3D concentration of MHP from the massive quasi-2D compositional space through classical batch-type experiments requires intensive efforts at the expense of tremendous time and energy.

Here we implement a high-throughput automated synthesis-characterization workflow based on a robotic pipetting platform to explore the quasi-2D MHP film system.[21,34,35] First, a series of quasi-2D precursor solutions with 95 different 2D:3D MHP ratios in the compositional space is prepared by accurately mixing both 2D and 3D solutions with a designed volume ratio (2D:3D) in each well of a microplate. By using an 8-channel pipet, the precursor solutions are drop-casted onto the glass substrates and subsequently heated (at 95 °C for 10 min) under an N_2 atmosphere (Figure S1, Supporting Information). As a result, an array of quasi-2D MHP films with 95 different 2D:3D compositions are fabricated.[36,37] The deposition and annealing process takes only 2 h in total and thus, significantly accelerates the fabrication sequence. The as-prepared MHP array is quickly transferred to an optical reader, where the PL spectra are collected from both the top and bottom sides of each film for 26 h (Figures S2 and S3, Supporting Information). This allows us to understand the general trend of phase distributions not only in the 2D:3D MHP compositional space but also in the vertical direction of each MHP film (**Figure 1a**).[20,38] Furthermore, the temporal decreases in PL intensity over time provide insights into the phase stability in each MHP film. From initial PL spectra, the $n = 1$ and 2 phases of 2D MHPs are dominant. This trend continues up to the $FAPbI_3$ ratio of ≈30%, where the emission from higher-n 2D phases ($n \geq 5$; peak wavelength >750 nm) and 3D $FAPbI_3$ MHPs (peak wavelength ≈820 nm) gradually emerge and become dominant by fur-

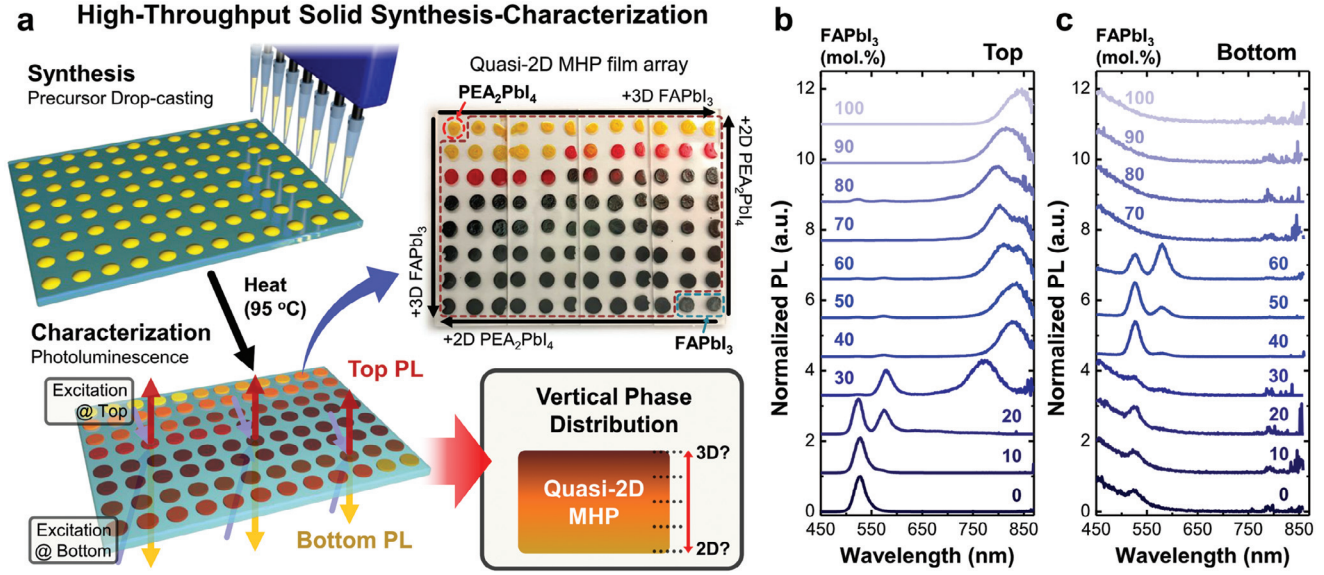

Figure 1. a) Schematics describing high-throughput synthesis and characterization of drop-casted PEA-FA quasi-2D MHP array. By using a fast-response optical reader, the PL spectra of the top- and bottom-side of the films are collected as a function of time, providing comprehensive insights into compositional and geometric phase distributions with corresponding phase stability of the film system. Representative b) top- and c) bottom-oriented initial PL spectra of the drop-casted quasi-2D MHP films with different 2D:3D composition ratios.

ther increasing the $FAPbI_3$ ratios (Figure 1b).[21,39] Note that, up to the $FAPbI_3$ ratio of ≈80%, the emergences of higher-*n* MHPs also involve the $n = 1$ and/or 2 phases, as evidenced by the corresponding PL at ≈525 and ≈580 nm, respectively (Figure S4, Supporting Information). This could be attributed to the disproportionation of intermediate phases (i.e., $n = 3$ and 4) and/or preferential formation in the crystallization process.[21,23] In contrast, only the $n = 1$ and 2 phases are observed from the bottom of the films, particularly up to 60% $FAPbI_3$ ratio (Figure 1c). Such a phase heterogeneity in the vertical direction has been explained by the surface-initiated MHP crystallization behavior; the 3D and higher-*n* MHP phases are first crystallized on the top of the precursor droplet (i.e., liquid-air interface) upon thermal annealing and the remaining 2D precursors are lastly crystallized on the bottom.[19,20,38] Note that the PL signals for higher-*n* and/or 3D-like phases could not be observed from the bottom surface due to their weak PL intensities and distinctive vertical phase separation with a richness of $n = 1$ and 2 phases at the bottom of the thick films.

The time-evolved automated PL characterization creates a massive dataset of emission spectra (95 compositions in one cycle × 52 times for 26 h (30 min interval) × top and bottom sides = 9880 individual PL spectra in total), which is impossible for humans to manually analyze each spectrum. To effectively analyze the entire dataset and thereby gain quantitative insights into the emergence of different phases in the quasi-2D MHP compositional space, non-negative matrix factorization (NMF)—an unsupervised machine learning (ML)–based multivariate analysis—is applied to the overall PL dataset.[35] This is an effective method for the separation of multidimensional datasets collected from the complex materials systems to rapidly extract the key characteristics of PL evolution associated with the MHP phases, thereby revealing the overall phase distributions of the quasi-2D MHP system.[21]

First, PL spectra of the top surface were deconvoluted by three components as an optimal condition,[35] which are associated with the emission of $n = 1$, $n = 2$ and high-*n* ($n \geq 5$), and 3D-like MHP phases, respectively (**Figure** 2a–c). The corresponding loading maps are combined in Figure 2d, clearly revealing a distinctive phase-emerging regime for each PL component in the quasi-2D MHP compositional space. The $n = 1$ phase exclusively emerges up to 20% $FAPbI_3$ ratio and then gradually disappears with increasing the ratio by 40%. Meanwhile, both $n = 2$ and high-*n* phases, which are previously reported to emerge along with each other,[21] are dispersed into two regions in the 2D:3D compositional space: a sharp spike and hill at the $FAPbI_3$ ratio of 20–40% and >60%, respectively. Note that, by using four components for NMF deconvolution,[35] the $n = 2$ phase is further separated out that only appears as a distinctive peak at the range of 20–40% $FAPbI_3$ ratio (Figure S5, Supporting Information), indicating that high-*n* phases emerge at higher $FAPbI_3$ concentrations.[12,16]

Interestingly, the 3D-like phases, with a PL peak centered at ≈820 nm, start to emerge at ≈35% $FAPbI_3$ ratio, showing a maximum PL intensity at the $FAPbI_3$ ratio of 40–50% where the PL emissions from other phases are insignificant in this composition range (a colored region in Figure 2d). That is, the 3D-like phase is dominant at this range of $FAPbI_3$ ratio in the quasi-2D MHP compositional space, which is not consistent with the ideal MHP stoichiometry at this compositional range—corresponds with $n = 2$ phase ($PEA_2FAPb_2I_7$). This can be attributed to the unbalanced crystallization kinetics between 2D, quasi-2D, and 3D-like phases, where the 3D-like phases can be more readily crystallized at the top surface than 2D MHPs as observed in the previous study.[20] It is likely that the stronger interaction between spacer cation and polar solvent retards the crystallization of 2D MHP phases;[21,24,26] the high dipole moment of spacer cation compared to FA cation can ascribe this.[40] Note that the 3D-like

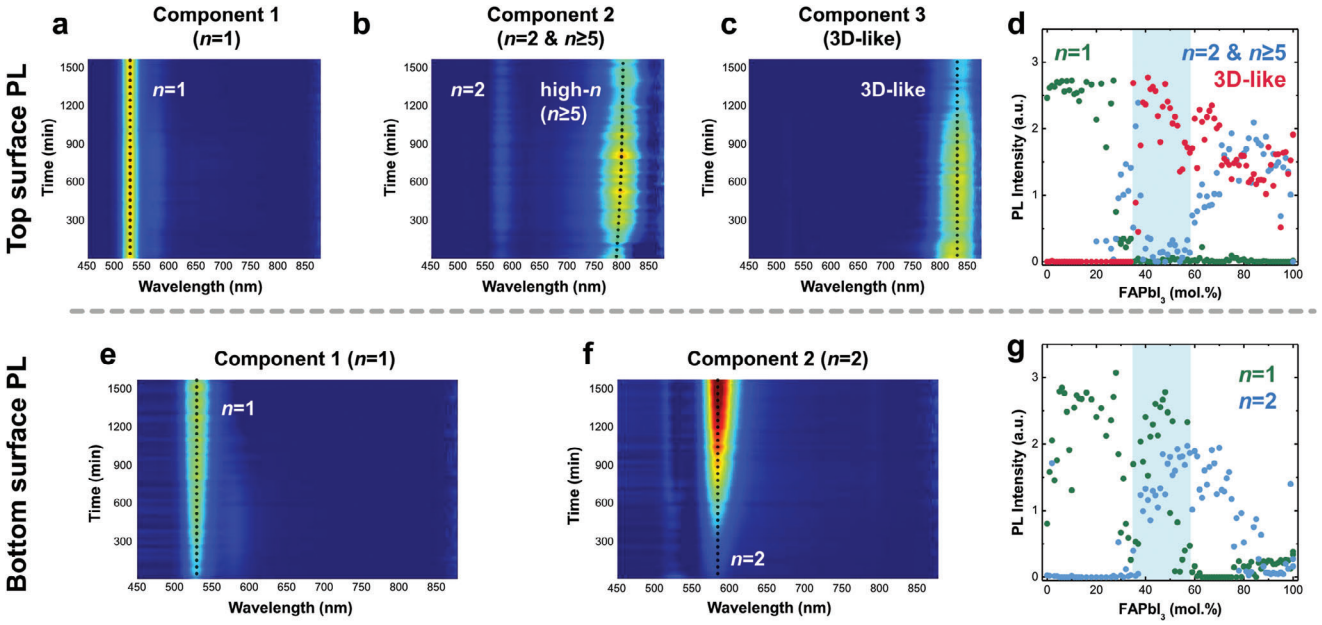

Figure 2. a–c) NMF-deconvolution of time-evolved PL components of top surface PL spectra. d) Combined top-side PL loading maps of the corresponding components. e,f) NMF-deconvoluted time-evolved PL components of bottom surface PL spectra. g) Combined bottom-side PL loading maps of the corresponding components.

phases have a structure where the crystal surface is passivated by 2D spacer cations protecting the MHP structure from external stresses, thereby manifesting better phase stability without compromising the excellent optoelectronic functionalities.[10,38] It should be also noted that the PL intensities of high-n and 3D-like phases (in Component 2 and 3, respectively) gradually decrease over time. These features are attributed to the temporal degradation of the corresponding crystallites upon exposure to ambient conditions during PL measurements, indicating those phases are less stable than n = 1 and 2 2D MHPs. Also, this indicates that the NMF analysis provides information regarding the overall stability behavior of the large compositional space of this binary system. In summary, the NMF analysis for top PL spectra provides a comprehensive understanding of how the phase distribution in quasi-2D MHP compositional space is regulated. Moreover, it reveals the optimal composition range that can be considered when designing these materials for desired functionalities.

Similarly, the bottom PL spectra are analyzed via NMF-deconvolution by two components, separating out the emission of $n = 1$ and $n = 2$ phases (i.e., PEA_2PbI_4 and $PEA_2FAPb_2I_7$) dispersed between 0–60 and 20–80% of $FAPbI_3$ ratios, respectively (Figure 2e–g). There is a region where both 2D MHP phases appear together, qualitatively consistent with the region where the 3D-like phases appeared at the top surface. It is observed that both PL emissions become stronger over time of the measurements. This suggests slow but spontaneous crystallization kinetics of the 2D phases at room temperature—from the remaining 2D precursors after forming the 3D-like phase at the top surface.

The crystallization sequence and the resulting phase constitutions in the quasi-2D MHP films, particularly in the vertical direction, can be altered by the chemical nature of the substrate. The MHP films deposited onto the UV/O_3 treated glass substrates—a nominal thickness of ≈818 nm confirmed by atomic force microscopy (Figure S6, Supporting Information)—exhibit a similar PL trend at both top and bottom sides with negligible emission of $n = 2$ phase (Figure S7–S9, Supporting Information). The mitigated vertical phase inhomogeneity could be attributed to the polar nature of the substrate after UV/O_3 treatment, which enhances solvent-substrate interaction and thereby release the spacer cations to participate in the overall crystallization process; Similar effect has been observed in quasi-2D MHP films incorporating polar precursors and/or ionic additives in the solutions. We compared the top and bottom PL of the quasi-2D MHP films spin-coated onto the substrates with different surface polarities, realized by the deposition of charge transport layers typically employed for device applications. Here, the SnO_2 electron transport layer and poly(triaryl amine) (PTAA) hole transport layer are representatively used to render polar and non-polar substrates, respectively. For two different 3D ratios majorly rendering 3D-like phases (40 and 50%), we observed the stronger PL intensities of the lower-n (i.e., $n = 1$ and 2) 2D MHP phases from the films deposited onto non-polar PTAA substrates (Figure S10, Supporting Information). These observations corroborate the hypothesis that the use of polar substrates can mitigate the vertical phase inhomogeneity. In addition, we note that the 3D-like phases start to emerge at lower $FAPbI_3$ ratios (≈25%) and become dominant up to ≈60%. Meanwhile, high-n phases develop in the similar compositional range observed from the MHP films formed onto the bare glass substrate (Figure 2b,d), together with a very weak $n = 1$ PL instead of that of the $n = 2$ phase. From the observations, we hypothesize that the $n = 2$ phase inhibits the emergence of the 3D-like α-$FAPbI_3$ phase, consistent with the observations during the early-stage crystallization dynamics.[21] Except for the behavior of the $n = 2$ phase, the overall phase distributions in the quasi-2D MHP compositional space are irrespective of the substrate.

Adjusting the precursor concentrations allows for thickness control over the MHP films, enabling replication of device-grade thickness (≈400 nm) across the quasi-2D MHP compositional space (Figures S11 and S12, Supporting Information). Furthermore, high-throughput explorations reveal that similar phase emergence behaviors are observed in the thinner quasi-2D MHP film arrays, which are also irrespective of the annealing temperatures and solvents (Figures S13–S16, Supporting Information). It is worth noting that the 3D-like phase in quasi-2D MHP films can be formed at 95 °C, even though the α-$FAPbI_3$ phase in pure $FAPbI_3$ films is thermodynamically preferred to be formed at >150 °C.[33] Presumably, the dimensional lattice confinements by spacer cation allow the favorable growth of the α-$FAPbI_3$ lattice as a form of the 3D-like phases. Summarizing these results confirms that the observed phase emergence behaviors can be universally replicated in any film system upon various synthesis parameter controls, which can be controlled in the high-throughput experimental workflow. This subsequently provides an essential understanding of how to achieve scalable fabrication of functional 3D-like phases in FA-based quasi-2D MHP systems, while minimizing vertical phase inhomogeneity in spin-coating-free fabrication processes such as inkjet printing and blade coating.

As a comparison, an array of PEA-methylammonium (MA) quasi-2D MHP thin film was also fabricated via high-throughput automated synthesis (Figure S17, Supporting Information). Time-evolved PL characterizations and the following NMF deconvolutions reveal that phase emergence behaviors in PEA-MA quasi-2d MHP compositional space are clearly different from those in PEA-FA counterparts (Figures S18 and S19, Supporting Information). Distinctive emergences of the intermediate phases (i.e., n = 3–5) are observed at 30–50% $MAPbI_3$ ratios, thereby rendering the sequential emergence of the higher-n phases with increasing the 3D ratios; this aligns with the previous studies that the quasi-3D MHP phases functional for PV application can be realized at the compositions >75% 3D.[26,27] As it was shown that, for the PEA-FA quasi-2D MHP system, the 3D-like phases are dominantly observed at this compositional range (i.e., 30–50% $FAPbI_3$), these results suggest that the observed phase emergence behaviors are an inherent nature of the PEA-FA quasi-2D MHPs. Thermodynamic preference associated with the formation of intermediate phases at the early stage of the crystallization process can result in such features.[21] This, in turn, justifies that the proposed high-throughput experimental workflow can be used as a universal approach for fundamental exploration in complex quasi-2D MHP compositional space.

To confirm the compatibility of the phase emergence behaviors observed from high-throughput experimentation, we manually fabricated the device-grade PEA-FA quasi-2D MHP films by spin coating (Figure S20, Supporting Information) at two different annealing temperatures (95 and 150 °C). The NMF deconvolution of resulting PL spectra reveals that the spin-coated thin films replicate the phase emergence behaviors observed in the high-throughput drop-casted MHP arrays (Figure S21, Supporting Information). The XRD patterns of thin films further agree with the phase emergence behaviors evidenced by PL analysis (Figure S22, Supporting Information). Note that the stronger α-$FAPbI_3$ (100) diffraction peak—showing a maximum intensity at 60% 3D ratio—is observed from the quasi-2D MHP films annealed at 95 °C, rather than 150 °C (Figure S23, Supporting Information). These observations once more suggest that in contrast to the fabrication of pure 3D $FAPbI_3$ film, lower annealing temperatures benefit the crystallinity of the 3D-like phase in PEA-FA quasi-2D MHP films. The surface morphology of spin-coated films was mapped using atomic force microscopy (AFM). The quasi-2D MHP films with the optimal range of 3D ratio exhibit smooth and uniform surface morphologies (Figure S24, Supporting Information) suited to device applications. We further explored the phase emergence behaviors in the spin-coated PEA-MA quasi-2D MHP films (Figures S25–S28, Supporting Information), which are again consistent with the trends in high-throughput observations that are distinctive from those in PEA-FA counterparts. These results corroborate that the proposed high-throughput automated experimental workflow directly explores the fundamental properties of the quasi-2D MHP films processed by device fabrication protocol, guaranteeing its universality and powerfulness in the acceleration of materials discovery.

Having understood the general tendency in phase distributions from PL, now we turn our focus onto the crystallographic structures of the quasi-2D MHP film system. To gain a comprehensive understanding of the crystal structures and orientation of the film system, HT-GIWAXS measurements are performed on all 96 MHP films in an array, giving high-throughput insights into phase distributions and orientations in a 2D:3D compositional space (**Figure 3**a). For measurements, three different incidence angles (φ)—0.05°, 0.1°, and 0.5°—are employed, which provides more information on crystal structures and preferential orientation from the surface (first few nanometers) to the bulk (several hundred nanometers) of each film in an array with increasing the incidence angle (Figure 3b).[41,42]

For all φ, the overall 2D GIWAXS patterns show the global trend of phase transformation—along their preferential orientations—in the quasi-2D MHP film systems as a function of 2D:3D compositional ratio (Figure 3c; Figures S29–S31, Supporting Information). Starting from the face-on oriented n = 1 2D phase at 0% $FAPbI_3$, the face-on oriented n = 2 phase emerges up to a $FAPbI_3$ ratio of 13%. Then the new vertically oriented crystallographic structure together with face-on oriented α-$FAPbI_3$ (100) phase (Q_r of ≈1.02 $Å^{-1}$) starts to develop and dominates up to 55% $FAPbI_3$ ratio.[28,38,43] Such a vertically oriented 2D MHP structure is anticipated to render excellent charge conduction properties.[32] Recall that, however, the corresponding PL emissions of other 2D phases except for n = 1 and 2 (specifically, n = 3 and 4) were not observed in this system (Figure 1b; Figure S2, Supporting Information). Meanwhile, a ring-shaped pattern at Q_r = ≈1.02 A^{-1} (random-oriented 3D α-$FAPbI_3$ phase) emerges from a 42% $FAPbI_3$ ratio. Furthermore, the random-oriented δ-$FAPbI_3$ (a ring pattern at Q_r = ≈0.86 $Å^{-1}$) phase emerges from ≈50% $FAPbI_3$ and becomes distinctive with an increasing ratio of $FAPbI_3$ to 100%. This is due to the thermodynamic stability of the non-perovskite phase at room temperature than the 3D MHP phase.[33] Note that there was a time interval between the fabrication of the film array and GIWAXS experiments, which manifests the α-to-δ phase transformation of the quasi-2D MHP films, particularly with high $FAPbI_3$ ratios. At high 3D ratios, the scattering patterns of the n = 1 and 2 2D MHPs exhibit ring-shape features, where the intensities are concentrated along the Q_z direction. This indicates that some of the 2D MHPs crystallites are randomly oriented in the film matrices, while considerable

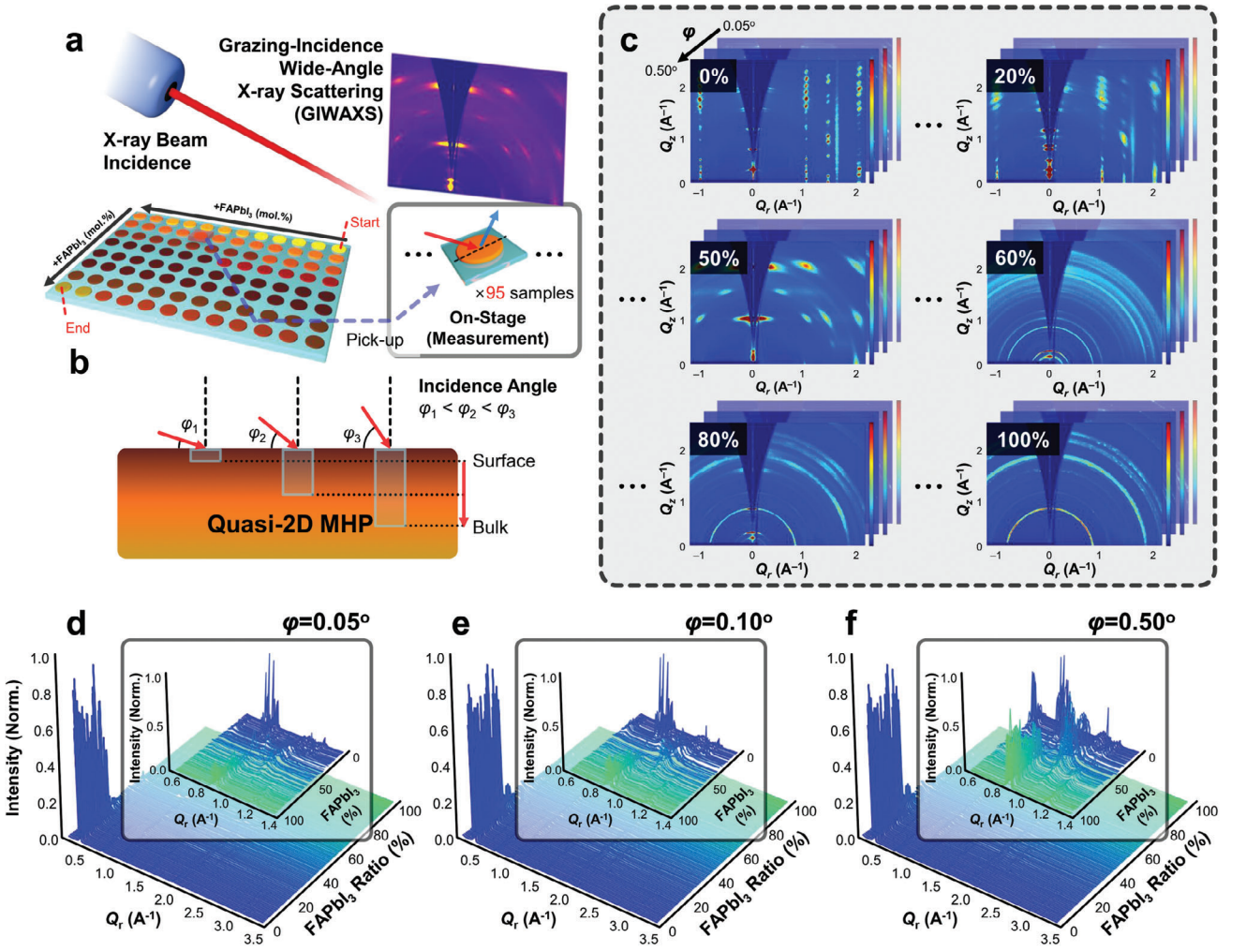

Figure 3. a) Schematics of HT-GIWAXS characterization of the drop-casted quasi-2D MHP film array. b) Incidence angle dependence in GIWAXS patterns. With increasing the incidence angle, more information associated with the bulk is obtained. c) Representative GIWAXS 2D patterns of the films with different 2D:3D composition ratios collected via HT-GIWAXS at three different incidence angles (φ). d–f) 1D GIWAXS profiles of the MHP films at φ of 0.05, 0.1, and 0.5°, respectively. Insets in (d–f) display the magnified 1D profiles of the films at Q_r of 0.53–1.4 Å^{-1}, showing other MHP-related diffraction patterns such as α- and δ-$FAPbI_3$ phases.

portions still exhibit face-on orientation. Note that, with increasing φ, the scattering patterns are more concentrated at the Q_z axis, indicating the face-on orientation. Although the absolute amount is not very high, vertically stacked 2D MHPs become more dominant at the film's bottom. The random-oriented growth of 2D MHPs can be attributed to the emergence of 3D-like phases, which restrict the aligned growth of the 2D sheets at the top surfaces.

To get quantitative insights into phase distributions in a 2D:3D compositional space, all the collected 2D GIWAXS patterns are converted to circular-averaged 1D profiles, giving 285 profiles in total (95 compositions × 3 different φ) as plotted in Figure 3d–f. We first manually analyze the representative GIWAXS 1D profiles collected at $\varphi = 0.5°$ for key $FAPbI_3$ ratios (Figures S32 and S33, Supporting Information). Evidently, there are noticeable changes in key diffraction peaks associated with the crystal structure of quasi-2D MHP phases (color-marked; Figures S32b and S33b, Supporting Information), as a function of $FAPbI_3$ compositional ratios. Specifically, the GIWAXS analysis reveals the gradual change of α-$FAPbI_3$ phase orientations from vertically aligned direction to random orientation within the $FAPbI_3$ compositional range of 55–59%, which also involves the emergence of δ-$FAPbI_3$ phase (Figure S33, Supporting Information). Overall, analyzing the entire 1D GIWAXS profiles can reveal a global trend of phase emergences in the quasi-2D MHP system with a quantitative sense.

However, practically, it requires tremendous effort and time for humans to analyze all these profiles individually (Figure S34, Supporting Information). To mitigate this challenge, we implemented an automated peak fitting function designed to trace the key diffraction peaks of quasi-2D MHP systems in each 1D GIWAXS profile. This significantly accelerates the analysis time. In fact, it only takes 5 minutes to fully analyze a dataset of 96 profiles and therefore, it takes 15 minutes in total to complete phase

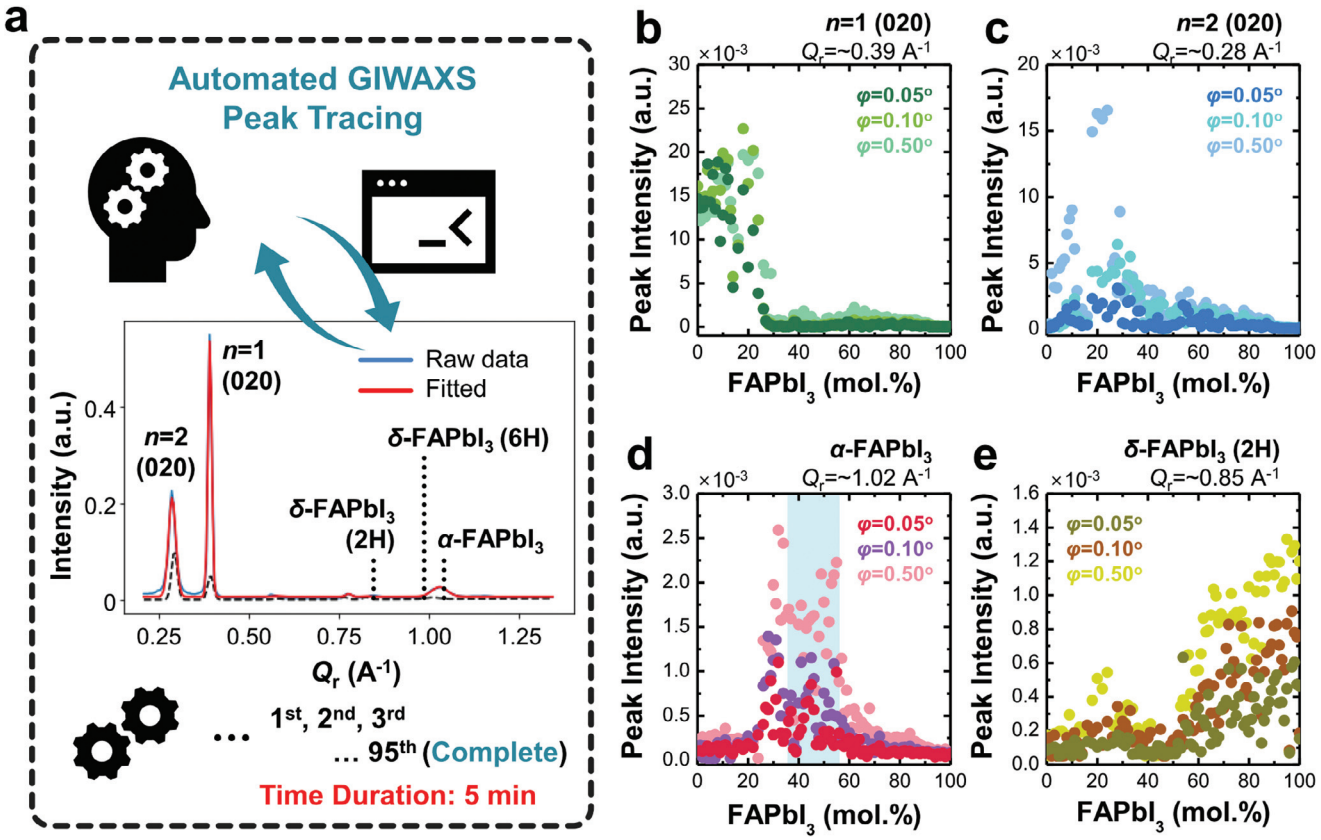

Figure 4. a) A schematic describing automated GIWAXS peak analysis workflow. This accelerates the overall analysis sequences, thereby revealing the qualitative insights of the distribution of each phase as a function of the 2D:3D composition ratio within 5 min. b–e) GIWAXS peak intensities of $n = 1$, $n = 2$, α- and δ-$FAPbI_3$ phases as a function of 2D:3D composition ratio, respectively.

identifications in the quasi-2D MHP compositional space at 3 different φ (**Figure** 4a).

Figure 4b–e exhibits the distribution profiles of $n = 1$, $n = 2$, α-$FAPbI_3$, and δ-$FAPbI_3$ phases as a function of $FAPbI_3$ compositional ratio at each φ, respectively. Similar to the PL trend, the strong (020) GIWAXS peak of the $n = 1$ phase ($Q_r = \approx 0.39$ Å^{-1}) appears at lower $FAPbI_3$ concentrations, which becomes 10 to 100 times weaker for the $FAPbI_3$ ratios of over 25% (Figure 4b). Within the low concentration of $FAPbI_3$ ratios, the peak intensity is irrespective of the φ, suggesting the $n = 1$ 2D phase is positioned at the top surface of the films. Note that, given the φ used for this study, the GIWAXS results only provide the crystallographic information about the first <1 μm from the foremost top of the film (thickness >4 μm); We cannot explore the crystal structure of the bottom side. The $n = 2$ phase exhibits a strong (020) GIWAXS peak at the $FAPbI_3$ compositional range from 10–40% (Figure 4c), which agrees with the trend seen in the PL spectra (Figure 2d). This peak becomes stronger with increasing the φ. Numerically, for the n = 2 MHP phase, a 7.75-fold increase in peak intensity is estimated when comparing the values collected from $\varphi = 0.5$ and 0.05o. In contrast, a nominal increase in peak intensity (2.35 times) is observed for the case of the α-FAPbI3 (100) phase (Figure 4d). This stark difference in the relative increments confirms that more $n = 2$ MHP crystallites are formed in the film interior.

The GIWAXS intensity of the α-$FAPbI_3$ (100) phase shows double peaks at 20–40 and 40–60% $FAPbI_3$ ratios and becomes stronger with an increase of φ (Figure 4d), where the compositional range of the latter region (color-marked) is consistent with that of the 3D-like phase in PL spectra. From the corresponding GIWAXS patterns collected at three φs, it is revealed that the α-$FAPbI_3$ (100) phase exhibits a face-on oriented alignment, as shown in the sharp Bragg spots in the 2D diffraction patterns (Figures S29—S33, Supporting Information). This indicates that the vertically aligned functional MHP structure can be extended to the film interior <1 μm, which is comparable with the actual device-level thickness. Given that the PL observations from the thin-film array where the distributions of the 3D-like phase are irrespective of the film thickness, the GIWAXS results suggest that the realization of highly oriented and stable α-$FAPbI_3$ that allows excellent vertical charge conduction is feasible, with some parametric optimizations in the film fabrication process. There are weak signals of corner-sharing δ-$FAPbI_3$ phase (Q_r = 0.99 Å^{-1}) at the $FAPbI_3$ compositional range of ≈50–56%—around the upper bound of the range where the 3D-like phase is observed (Figure S35, Supporting Information). This infers that the 3D-like phase can also undergo degradation at this range, which is, however, not very significant. Meanwhile, the GIWAXS intensity of the δ-$FAPbI_3$ phase—because of the deformation of α-phase due to its thermodynamic instability—starts to emerge at a 60%

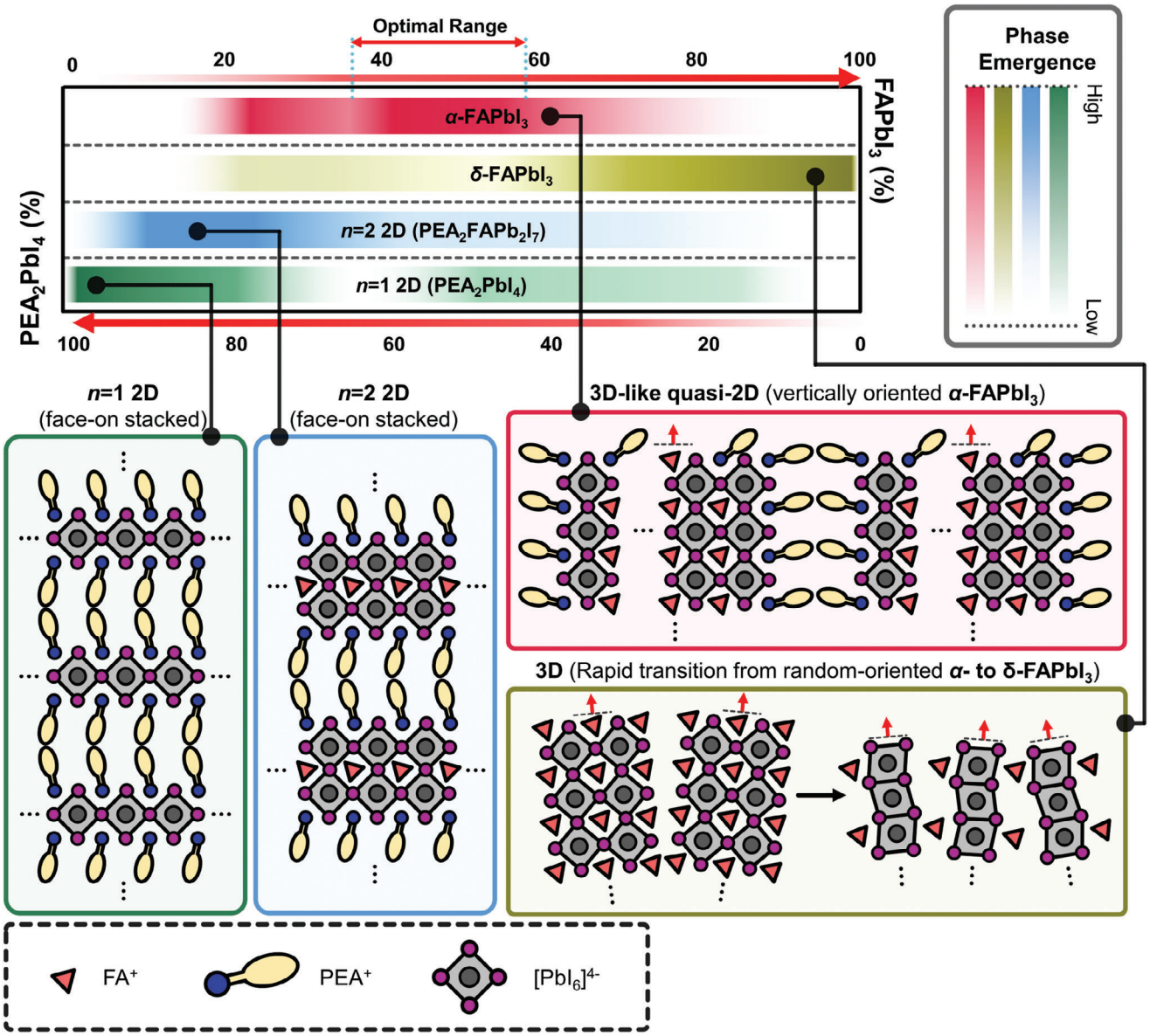

Figure 5. Phase distributions and their corresponding crystallographic structures in PEA-FA quasi-2D MHP film system deduced by HT-GIWAXS characterization.

$FAPbI_3$ ratio and gradually becomes stronger with further increasing the $FAPbI_3$ concentration (Figure 4e).

Overall, the observations from HT-GIWAXS characterizations clearly show a distinctive phase-emerging region with the corresponding crystallographic structure for each phase (**Figure 5**). The results also reveal that the stable, vertically oriented α-$FAPbI_3$ phase as a 3D-like MHP form can be exclusively formed at the $FAPbI_3$ compositional range of ≈35–55%, consistent with the observation in PL analysis. Indeed, we observed that the highest PV performances—particularly rendering the highest short-circuit current densities (J_{SC}s)—are realized from the unoptimized devices employing the quasi-2D MHP with 60 and 70% 3D ratio, closest to the optimal composition (Figures S36 and S37, Supporting Information). These observations clearly align with the expectation based on the high-throughput and selected-film characterizations. These findings clearly provide quantitative evidence for uniting the spread notions regarding the optimal quasi-2D composition,[22,24,25,44] which has no consensus to date—from its first photovoltaic applications.[45]

Recall that the phase distribution of the 3D-like MHP with excellent optoelectronic functionalities shows a similar trend when the thickness of the film is adjusted to the device-grade-thick level. This implies that our accelerated materials exploration strategy based on high-throughput material synthesis and characterization workflow provides fundamental insights and universal design principles that can be directly implemented into the scalable, mass-producible device manufacturing sequence. Subsequently, this will allow for accelerating the optimization

process to realize efficient and stable solution-processable MHP optoelectronics on an industrial scale.

3. Outlook

In summary, the evolution of phase emergences, distributions, and their stability assessments in the quasi-2D MHP films are systematically explored via high-throughput automated experimental workflow. From the analysis of high throughput PL spectroscopy, by implementing the unsupervised ML algorithm, both the compositional and geometric changes of MHP phase heterogeneities in the quasi-2D system are expeditiously quantified. This study not only facilitates the acceleration of materials exploration and discovery sequences but also provides a comprehensive understanding of the complex quasi-2D system in an efficient manner. It is revealed that stable 3D-like α-$FAPbI_3$ MHP phases exclusively emerge at a specific 2D:3D compositional range (35-55% of $FAPbI_3$ ratio). Ideally, this composition ratio corresponds with the $n = 2$ 2D MHP stoichiometry (at 50% $FAPbI_3$, $PEA_2FAPb_2I_7$), which is structurally not the case in this system. This suggests the desired functionalities in actual materials systems can appear far away from the expectations driven by conventional chemical knowledge based on stoichiometric calculations.

A comprehensive investigation of the crystallographic structures and orientations of the quasi-2D MHP systems is realized via HT-GIWAXS characterizations, where the integration of an automated peak analysis function significantly accelerates the quantitative phase identifications. It is identified that the developed 3D-like phases observed in PL analysis indeed consist of α-$FAPbI_3$ MHPs with vertical lattice orientation—confirmed to provide the highest J_{SC}s in PV devices by favorable vertical charge conductions—and exhibit outstanding phase stability. In stark contrast, the quasi-2D MHPs with FA-rich compositions are readily transformed to the photo-inactive δ-phase, thereby failing the functionalities over time. Collectively, the high-throughput explorations of complex quasi-2D systems uncover the optimal 2D:3D compositional ratios exhibiting the desired functionalities and crystallographic structures, thereby providing a generalized guideline for designing promising optoelectronic functionalities. The high-throughput workflow utilized in this work enables systematic and concurrent identification of phase emergence behaviors and their crystallographic structures in a complex quasi-2D MHP compositional space, which has not been achieved by other high-throughput approaches so far.[21,31,34–37] In addition, our research reveals a crucial and all-encompassing principle that must be considered when designing phases of a material system. This principle can be readily applied in various manufacturing processes that can be expanded without limitations.

4. Experimental Section

Materials: Formamidinium iodide (FAI; Greatcellsolar, >99.99%), lead (II) iodide (PbI_2; Fisher Scientific, 99.999% ultra-dry, metals basis), phenethylammonium iodide (PEAI; Sigma-Aldrich, 98%), *N*,*N*-dimethylformamide (DMF; Sigma-Aldrich, 99.8% anhydrous) were purchased and used without further purification.

High-throughput Robotic Synthesis of Quasi-2D MHP Film Array: 2D PEA_2PbI_4n (0.7 M) and 3D $FAPbI_3$ (0.7 M) precursors in DMF solutions were prepared by dissolving stoichiometric amounts of materials under N_2 atmosphere and stirred for 2 h at room temperature. Then the solutions were transferred to a pipetting robot platform (Opentrons, OT-2) in the N_2 atmosphere.

The overall experimental setup for a high-throughput robotic synthesis platform is shown in Figure S1a, Supporting Information. By using a 300 µL-capacity single-channel pipet, 50 µL of quasi-2D precursor solutions with a targeted 2D:3D ratio, were filled in each well of a microplate (Figure S1b, Supporting Information). Then, by using a 20 µL-capacity 8-channel pipet, 8 µL of the prepared solutions were dispensed onto the glass substrate placed on the heating module with a fixed temperature of 95 °C. The droplets were crystallized at 95 °C for 10 min, resulting in crystallized quasi-2D MHP films with a nominal diameter of ≈8 mm. Similarly, for making thin quasi-2D MHP film array, the UV/O_3-treated glass substrates were used and 0.7 µL of the precursor solutions were dispensed onto the substrate while maintaining the other synthesis parameters constant. The thickness of the quasi-2D MHP films was confirmed by using non-contact mode atomic force microscopy (Oxford Instrument, Cypher).

Time-evolved PL Measurements: The synthesized quasi-2D MHP film array was quickly mounted to a hybrid multi-mode optical reader (BioTek, Cytation 5) and the time-evolved PL spectra (1 nm step) of each film were collected from both the bottom and top of the substrate with an excitation wavelength of 365 nm. In the measurement workflow designed by Gen5 software, the spot size of the excitation beam was adjusted to be ≈3 mm in diameter. This allows us to selectively excite the center of the films in the array, thereby excluding the PL signals collected from the edges of the films having different phase constitutions. The emission spectra from each film spot were obtained as one "read" cycle every 15 min for the 96 films. The read cycle was repeated for >1500 min (i.e., 26 h). A PL read sequence was designed for the alternating scan of both the top and bottom substrate, thereby obtaining the time-evolved PL spectra from both top and bottom over time. This resulted in the actual time interval between the read cycles at each position being 30 min.

PL Data Analysis: NMF data analysis was performed on Google Colab using Python 3.6 and the sci-kit-learn 0.22.1 library. The code was available in the following link (google Colab):https://drive.google.com/file/d/1GHGC4xGaZ2VnnWKBnRcgp6fPXQY0OspQ/view?usp=sharing

HT-GIWAXS Characterizations and Data Analysis: HT-GIWAXS experiments of quasi-2D MHP films were done at beamline 11-BM at Brookhaven National Laboratory. The samples were measured at the three incident angles (φ) of 0.05, 0.1, and 0.5 degrees with a 10 s exposure time. The X-ray beam had an energy of 13.5 keV, 0.2 mm (height) × 0.05 mm (width) size, 1 mrad divergence, and an energy resolution of 0.7%. Data were initially analyzed building on the SciAnalysis package provided by the beamline. Automated GIWAXS peak fitting function designed on Google Colab using Python 3.6 and Lmfit 1.1.0. and used for the sets of circularly integrated 1D GIWAXS profiles. The code was available in the following links (google Colab): https://colab.research.google.com/drive/1H1dqAvglpoMuVUKUJpkCBz7NVh6D4tf5?usp=sharing
https://colab.research.google.com/drive/16hMSQ7oP94T5ReOsnc5Jixp0zpb6v4FQ?usp=sharing

Solar Cell Fabrication and Characterization: 1 × 1 $inch^2$ glass substrates with fluorine-doped tin oxide (FTO) patterns were cleaned under an ultrasonication bath by a 2% mucasol (Schülke) solution, deionized water, acetone, and 2-propanol for 15 min each. They were then thoroughly dried with a nitrogen gun. Using the cleaned substrates, UV-ozone treatment was performed for 15 min and then a mixed solution of 800 µl titanium di-isopropoxide bis(acetylacetonate) (75% in 2-propanol, Merck) and 10.8 mL anhydrous ethanol was sprayed on a hot plate to deposit TiO_2 compact layers. We note that a Sparmax spray gun with a flow rate (4 L min^{-1}) of oxygen carrier gas was used and the hot plate temperature was set to 450 °C and maintained for 30 min after spraying. TiO_2 mesoporous layers were then deposited by spin-coating at 4000 rpm for 10 s with a 150 mg mL^{-1} solution of a commercial TiO_2 paste (Sigma Aldrich) diluted in anhydrous ethanol. The substrates were dried at a temperature of 100 °C for 10 min to remove the volatile solvent. They were thereafter annealed at 450 °C for 30 min and subsequently cooled down to 150 °C before being transferred to a nitrogen-filled glove box (<1 ppm O_2 and H_2O)

for perovskite deposition. 1 M perovskite solutions of 3D $FAPbI_3$ and 2D PEA_2PbI_4 were prepared in a nitrogen-filled glove box by dissolving the salts in a mixed solvent of DMF and DMSO (4:1, v/v) and then they were mixed at a varied ratio (10:0, 9:1, 8:2, 7:3, 6:4, and 0:10, v/v) before use. The as-prepared solutions were then dropped to the TiO_2-deposited substrates (90 µL volume) and spin-coated at 4000 rpm for 50 s. After that, the substrates were annealed at 95 °C for 15 min to crystallize perovskite films. Spiro-OMeTAD was then spun at 3000 rpm for 30 s with no annealing, whose solution was prepared by dissolving 140 mg of spiro-OMeTAD (1-Material) in 1.538 mL of chlorobenzene and then adding 25 uL of a 1.8 M Li-TFSI solution in acetonitrile, 14 uL of a 0.25 M FK-209 Co (III) TFSI salt (Sigma-Aldrich) solution in acetonitrile (Sigma-Aldrich, anhydrous 99.8%), and 55 uL of 4 *tert*-butylpyridine (Sigma–Aldrich, 98%). Finally, 50 nm thick gold was evaporated atop the Spiro-OMeTAD-deposited substrates.

Characteristic *J–V* curves were collected with a Fluxim solar simulator by which standard 1 sun-light (AM 1.5 G, 100 mW cm^{-2}) was illuminated to the fabricated devices and voltage was scanned backward and forward at a range of −0.5–1.4 V with a rate of 50 mV s^{-1}. The stabilized PCE was taken from a maximum power point (MPP) tracking for 3 min.

Materials Characterizations: XRD patterns of the films were collected by using a high-resolution X-ray diffractometer (Malvern Panalytical, Empyrean). AFM surface morphology profiles of the films were collected by using an atomic-force microscope (Park Systems, XE-100).

Supporting Information

Supporting Information is available from the Wiley Online Library or from the author.

Acknowledgements

J.Y. and M.A. acknowledge support from the National Science Foundation (NSF), Award Number No. 2043205, and Alfred P. Sloan Foundation, award No. FG-2022-18275. J.H. acknowledges the Department of Education Graduate Assistance in Areas of National Need (GAANN) program at Georgia Institute of Technology (Award #P200A180075). This research used the CMS 11-BM Beamline of the National Synchrotron Light Source II, a U.S. Department of Energy (DoE) Office Science User Facility operated for the DOE Office of Science by Brookhaven National Laboratory under Contract DE-SC0012704. The authors sincerely appreciate Ruipeng Li for his contributions to HT-GIWAXS experiments.

Conflict of Interest

The authors declare no conflict of interest.

Data Availability Statement

The data that support the findings of this study are available in the supplementary material of this article.

Keywords

accelerated materials discovery, grazing-incidence wide-angle X-ray scattering, high-throughput synthesis, quasi-2D perovskites

Received: May 29, 2024
Revised: July 9, 2024
Published online: August 9, 2024

[1] J. Park, J. Kim, H. S. Yun, M. J. Paik, E. Noh, H. J. Mun, M. G. Kim, T. J. Shin, S. I. Seok, *Nature* **2023**, *616*, 724.
[2] Y. Jiang, C. Sun, J. Xu, Li, M. Cui, X. Fu, Y. Liu, Y. Liu, H. Wan, K. Wei, T. Zhou, W. Zhang, Y. Yang, J. Yang, C. Qin, S. Gao, J. Pan, Y. Liu, S. Hoogland, E. H. Sargent, J. Chen, M. Yuan, *Nature* **2022**, *612*, 679.
[3] J. S. Kim, J. M. Heo, G. S. Park, S. J. Woo, C. Cho, H. J. Yun, D. H. Kim, J. Park, S. C. Lee, S. H. Park, E. Yoon, N. C. Greenham, T. W. Lee, *Nature* **2022**, *611*, 688.
[4] D. Ma, K. Lin, Y. Dong, H. Choubisa, A. H. Proppe, D. Wu, Y. K. Wang, B. Chen, P. Li, J. Z. Fan, F. Yuan, A. Johnston, Y. Liu, Y. Kang, Z. H. Lu, Z. Wei, E. H. Sargent, *Nature* **2021**, *599*, 594.
[5] H. T. Zhang, T. J. Park, I. A. Zaluzhnyy, Q. Wang, S. N. Wadekar, S. Manna, R. Andrawis, P. O. Sprau, Y. F. Sun, Z. Zhang, C. Z. Huang, H. Zhou, Z. Zhang, B. Narayanan, G. Srinivasan, N. Hua, E. Nazaretski, X. J. Huang, H. F. Yan, M. Y. Ge, Y. S. Chu, M. J. Cherukara, M. V. Holt, M. Krishnamurthy, O. G. Shpyrko, S. K. R. S. Sankaranarayanan, A. Frano, K. Roy, Ramanathan, *Nat. Commun.* **2020**, *11*, 2245.
[6] Y. H. Kim, J. Park, S. Kim, J. S. Kim, H. Xu, S. H. Jeong, B. Hu, T. W. Lee, *Nat. Nanotechnol.* **2022**, *17*, 590.
[7] L. Duan, D. Walter, N. Chang, J. Bullock, D. Kang, S. P. Phang, K. Weber, T. White, D. Macdonald, K. Catchpole, H. Shen, *Nat. Rev. Mater.* **2023**, *8*, 261.
[8] L. Meng, J. You, Y. Yang, *Nat. Commun.* **2018**, *9*, 5265.
[9] C. C. Boyd, R. Cheacharoen, T. Leijtens, M. D. McGehee, *Chem. Rev.* **2019**, *119*, 3418.
[10] J. W. Lee, Z. Dai, T. H. Han, C. Choi, S. Y. Chang, S. J. Lee, N. De Marco, H. Zhao, P. Sun, Y. Huang, Y. Yang, *Nat. Commun.* **2018**, *9*, 3021.
[11] X. T. Li, J. M. Hoffman, M. G. Kanatzidis, *Chem. Rev.* **2021**, *121*, 2230.
[12] C. M. M. Soe, G. P. Nagabhushana, R. Shivaramaiah, H. H. Tsai, W. Y. Nie, J. C. Blancon, F. Melkonyan, D. H. Cao, B. Traore, L. Pedesseau, M. Kepenekian, C. Katan, J. Even, T. J. Marks, A. Navrotsky, A. D. Mohite, C. C. Stoumpos, M. G. Kanatzidis, *Proc. Natl. Acad. Sci. USA* **2019**, *116*, 58.
[13] H. Lai, D. Lu, Z. Xu, N. Zheng, Z. Xie, Y. Liu, *Adv. Mater.* **2020**, *32*, 2001470.
[14] X. M. Zhao, M. L. Ball, A. Kakekhani, T. R. Liu, A. M. Rappe, Y. L. Loo, *Nat. Commun.* **2022**, *13*, 3970.
[15] F. Zhang, S. Y. Park, C. Yao, H. Lu, S. P. Dunfield, C. Xiao, S. Ulicna, X. Zhao, L. Du Hill, X. Chen, X. Wang, L. E. Mundt, K. H. Stone, L. T. Schelhas, G. Teeter, S. Parkin, E. L. Ratcliff, Y. L. Loo, J. J. Berry, M. C. Beard, Y. Yan, B. W. Larson, K. Zhu, *Science* **2022**, *375*, 71.
[16] T. He, S. Li, Y. Jiang, C. Qin, M. Cui, L. Qiao, H. Xu, J. Yang, R. Long, H. Wang, M. Yuan, *Nat. Commun.* **2020**, *11*, 1672.
[17] J. Yang, D. K. LaFollette, B. J. Lawrie, A. V. Ievlev, Y. Liu, K. P. Kelley, S. V. Kalinin, J. P. Correa-Baena, M. Ahmadi, *Adv. Energy Mater.* **2023**, *13*, 2202880.
[18] S. Macpherson, T. A. S. Doherty, A. J. Winchester, S. Kosar, D. N. Johnstone, Y. H. Chiang, K. Galkowski, M. Anaya, K. Frohna, A. N. Iqbal, S. Nagane, B. Roose, Z. Andaji-Garmaroudi, K. W. P. Orr, J. E. Parker, P. A. Midgley, K. M. Dani, S. D. Stranks, *Nature* **2022**, *607*, 294.
[19] S. Chen, X. Xiao, B. Chen, L. L. Kelly, J. Zhao, Y. Lin, M. F. Toney, J. Huang, *Sci. Adv.* **2021**, *7*, eabb2412.
[20] Y. Lin, Y. Fang, J. Zhao, Y. Shao, S. J. Stuard, M. M. Nahid, H. Ade, Q. Wang, J. E. Shield, N. Zhou, A. M. Moran, J. Huang, *Nat. Commun.* **2019**, *10*, 1008.
[21] J. Yang, B. J. Lawrie, S. V. Kalinin, M. Ahmadi, *Adv. Energy Mater.* **2023**, *13*, 2302337.
[22] Y. Zhang, N. G. Park, *ACS Energy Lett.* **2022**, *7*, 757.
[23] K. Wang, Z. Y. Lin, Z. Zhang, L. Jin, K. Ma, A. H. Coffey, H. R. Atapattu, Y. Gao, J. Y. Park, Z. Wei, B. P. Finkenauer, C. Zhu, X. Meng, S. N. Chowdhury, Z. Chen, T. Terlier, T. H. Do, Y. Yao, K. R. Graham, A.

Boltasseva, T. F. Guo, L. Huang, H. Gao, B. M. Savoie, L. Dou, *Nat. Commun.* **2023**, *14*, 397.
[24] A. Caiazzo, R. A. J. Janssen, *Adv. Energy Mater.* **2022**, *12*, 2202830.
[25] A. H. Coffey, S. J. Yang, m. Gomez, B. P. Finkenauer, T. Terlier, C. Zhu, L. Dou, *Adv. Energy Mater.* **2023**, *13*, 2201501.
[26] X. Zhang, R. Munir, Z. Xu, Y. Liu, H. Tsai, W. Nie, J. Li, T. Niu, D. M. Smilgies, M. G. Kanatzidis, A. D. Mohite, K. Zhao, A. Amassian, S. F. Liu, *Adv. Mater.* **2018**, *30*, 1707166.
[27] C. M. M. Soe, W. Y. Nie, C. C. Stoumpos, H. Tsai, J. C. Blancon, F. Z. Liu, J. Even, T. J. Marks, A. D. Mohite, M. G. Kanatzidis, *Adv. Energy Mater.* **2018**, *8*, 1700979.
[28] N. Zhou, Y. Shen, L. Li, S. Tan, N. Liu, G. Zheng, Q. Chen, H. Zhou, *J. Am. Chem. Soc.* **2018**, *140*, 459.
[29] C. Sun, Y. Jiang, M. Cui, L. Qiao, J. Wei, Y. Huang, L. Zhang, T. He, S. Li, H. Y. Hsu, C. Qin, R. Long, M. Yuan, *Nat. Commun.* **2021**, *12*, 2207.
[30] L. Quan, D. X. Ma, Y. B. Zhao, O. Voznyy, H. F. Yuan, E. Bladt, J. Pan, F. P. G. de Arquer, R. Sabatini, Z. Piontkowski, A. H. Emwas, P. Todorovic, R. Quintero-Bermudez, G. Walters, J. Z. Fan, M. X. Liu, H. R. Tan, M. I. Saidaminov, L. Gao, Y. Y. Li, D. H. Anjum, N. N. Wei, J. Tang, D. W. McCamant, M. B. J. Roeffaers, S. Bals, J. Hofkens, O. M. Bakr, Z. H. Lu, E. H. Sargent, *Nat. Commun.* **2020**, *11*, 170.
[31] S. L. Sanchez, Y. Tang, B. Hu, J. Yang, M. Ahmadi, *Matter* **2023**, *6*, 2900.
[32] L. Yan, J. Ma, P. Li, S. Zang, L. Han, Y. Zhang, Y. Song, *Adv. Mater.* **2022**, *34*, 2106822.
[33] V. L. Pool, B. Dou, D. G. Van Campen, T. R. Klein-Stockert, F. S. Barnes, S. E. Shaheen, M. I. Ahmad, M. F. van Hest, M. F. Toney, *Nat. Commun.* **2017**, *8*, 14075.
[34] K. Higgins, S. M. Valleti, M. Ziatdinov, S. V. Kalinin, M. Ahmadi, *ACS Energy Lett.* **2020**, *5*, 3426.
[35] K. Higgins, M. Ziatdinov, S. V. Kalinin, M. Ahmadi, *J. Am. Chem. Soc.* **2021**, *143*, 19945.
[36] J. Zhang, S. Langner, J. Wu, C. Kupfer, L. Luer, W. Meng, B. Zhao, C. Liu, M. Daum, A. Osvet, N. Li, M. Halik, T. Stubhan, Y. Zhao, J. Hauch, C. J. Brabec, *ACS Energy Lett.* **2022**, *7*, 70.
[37] J. Zhang, J. Wu, S. Langner, B. Zhao, Z. Xie, J. A. Hauch, H. A. Afify, A. Barabash, J. Luo, M. Sytnyk, W. Meng, K. Zhang, C. Liu, A. Osvet, N. Li, M. Halik, W. Heiss, Y. Zhao, C. J. Brabec, *Adv. Funct. Mater.* **2022**, *32*, 2207101.
[38] A. Z. Chen, M. Shiu, J. H. Ma, M. R. Alpert, D. Zhang, B. J. Foley, D. M. Smilgies, S. H. Lee, J. J. Choi, *Nat. Commun.* **2018**, *9*, 1336.
[39] F. Ma, J. Li, W. Li, N. Lin, L. Wang, J. Qiao, *Chem. Sci.* **2017**, *8*, 800.
[40] H. Song, J. Yang, W. H. Jeong, J. Lee, T. H. Lee, J. W. Yoon, H. Lee, A. J. Ramadan, R. D. J. Oliver, S. C. Cho, S. G. Lim, J. W. Jang, Z. Yu, J. T. Oh, E. D. Jung, M. H. Song, S. H. Park, J. R. Durrant, H. J. Snaith, S. U. Lee, B. R. Lee, H. Choi, *Adv. Mater.* **2023**, *35*, 2209486.
[41] C. A. R. Perini, E. Rojas-Gatjens, M. Ravello, A. F. Castro-Mendez, J. Hidalgo, Y. An, S. Kim, B. Lai, R. Li, C. Silva-Acuna, J. P. Correa-Baena, *Adv. Mater.* **2022**, *34*, 2204726.
[42] J. Hidalgo, C. A. R. Perini, A. F. Castro-Mendez, D. Jones, H. Kobler, B. Lai, R. P. Li, S. J. Sun, A. Abate, J. P. Correa-Baena, *ACS Energy Lett.* **2020**, *5*, 3526.
[43] C. Liang, H. Gu, Y. D. Xia, Z. Wang, X. T. Liu, J. M. Xia, S. W. Zuo, Y. Hu, X. Y. Gao, W. Hui, L. F. Chao, T. T. Niu, M. Fang, H. Lu, H. Dong, H. Yu, S. Chen, X. Q. Ran, L. Song, B. X. Li, J. Zhang, Y. Peng, G. S. Shao, J. P. Wang, Y. H. Chen, G. C. Xing, W. Huang, *Nat. Energy* **2021**, *6*, 38.
[44] J. Liang, Z. Zhang, Q. Xue, Y. Zheng, X. Wu, Y. Huang, X. Wang, C. Qin, Z. Chen, C. C. Chen, *Energy Environ. Sci.* **2022**, *15*, 296.
[45] I. C. Smith, E. T. Hoke, D. Solis-Ibarra, M. D. McGehee, H. I. Karunadasa, *Angew. Chem., Int. Ed.* **2014**, *53*, 11232.